J. Fluid Mech. (1993), *vol.* 253, *pp.* 485–507

Spatial simulation of secondary instability in plane channel flow: comparison of K- and H-type disturbances

By E. M. SAIKI[1], S. BIRINGEN[1]†, G. DANABASOGLU[1]‡
AND C. L. STREETT[2]

[1] Department of Aerospace Engineering Sciences, University of Colorado, Boulder, CO 80309, USA

[2] Theoretical Aerodynamics Branch, Fluid Dynamics Division, NASA/Langley Research Center, Hampton, VA 23665, USA

(Received 29 April 1992 and in revised form 30 January 1993)

This study involves a numerical simulation of spatially evolving secondary instability in plane channel flow. The computational algorithm integrates the time-dependent, three-dimensional, incompressible Navier–Stokes equations by a mixed finite-difference/spectral technique. In particular, we are interested in the differences between instabilities instigated by Klebanoff (K-) type and Herbert (H-) type inflow conditions, and in comparing the present spatial results with previous temporal models. It is found that for the present inflow conditions, H-type instability is biased towards one of the channel walls, while K-type instability evolves on both walls. For low initial perturbation amplitudes, H-type instability exhibits higher growth rates than K-type instability while higher initial amplitudes lead to comparable growth rates of both H- and K-type instability. In H-type instability, spectral analysis reveals the presence of the subharmonic two-dimensional mode which promotes the growth of the three-dimensional spanwise and fundamental modes through nonlinear interactions. An intermodal energy transfer study demonstrates that there is a net energy transfer from the three-dimensional modes to the two-dimensional mode. This analysis also indicates that the mean mode transfers net energy to the two-dimensional subharmonic mode and to the three-dimensional modes.

1. Introduction

Secondary instability in wall-bounded shear flows was first identified in the boundary-layer experiments of Klebanoff, Tidstrom & Sargent (1962), in which a vibrating ribbon was used to create disturbances in the form of initially two-dimensional Tollmien–Schlichting (T–S) waves that amplify (or decay) as they travel downstream. Klebanoff *et al.* (1962) observed that the ribbon-induced disturbances develop into three-dimensional Λ-shaped structures (Λ-vortices) arranged in a distinctive pattern periodic in x and z, i.e. repeating from $(x,z)\rightarrow(x+\lambda_x, z+\lambda_z)$; here, x and z represent the streamwise and spanwise coordinates, respectively, and λ_x and λ_z are the corresponding fundamental wavelengths of the disturbances. This type of secondary instability is known as K-type (Klebanoff-type) or fundamental instability.

---

† Author to whom correspondence should be addressed.

‡ Present address: National Center for Atmospheric Research, PO Box 3000, Boulder, CO 80307, USA.

More recently, in his theoretical studies Herbert (1983*a*, *b*) found that high-amplitude, two-dimensional disturbances lead to K-type instability, while low-amplitude, two-dimensional disturbances promote a subharmonic secondary instability. The existence of the latter, which is also referred to as H-type (Herbert-type) instability, was confirmed by experimental observations in boundary layers (Kachanov, Kozlov & Levchenko 1978; Kachanov & Levchenko 1984; Saric, Kozlov & Levchenko 1984) and is characterized by the staggered arrangement of the Λ-vortices, i.e. a pattern which is invariant to coordinate transformations of the type $(x, z) \rightarrow (x+2\lambda_x, z+\lambda_z)$. In channel flow experiments, although K-type instability was observed to evolve naturally (Nishioka, Iida & Ichikawa 1975; Nichioka, Asai & Iida 1980, 1981; Kozlov & Ramazanov 1984), H-type instability was obtained only in the presence of a forced subharmonic disturbance (Ramazanov 1985).

The evolutionary characteristics of the two types of secondary instability have been examined through numerical simulations of both boundary-layer and channel flows. Several review articles (Herbert 1991; Kleiser & Zang 1991) contain a summary of previous computational work. In the majority of these simulations, a two-dimensional disturbance wave and a three-dimensional oblique wave pair were used as the inflow conditions for spatial models or as initial conditions for temporal models. One of the interesting characteristics of secondary instability in channel flows is the biased initiation of transition towards one wall in H-type instability in contrast to the concurrent activity at both walls in K-type instability (Herbert 1983*a*; May & Kleiser 1985; Singer, Ferziger & Reed 1987; Singer, Reed & Ferziger 1989). In their temporal boundary-layer simulations, Laurien & Kleiser (1989) compared H- and K-type instability, each excited by a low-amplitude (1.5% of the free-stream velocity) two-dimensional T–S wave and an oblique wave pair with a combined amplitude of 0.1%. They observed that under these conditions the inception of K-type instability was delayed in comparison with H-type, however H-type instability was not as strong as K-type. Similarly, in the temporal simulations of Zang & Hussaini (1985) and Krist & Zang (1987), H-type instability in plane channel flow was weaker than K-type under various initial conditions, i.e. for different amplitudes of the two- and three-dimensional initial disturbances, different Reynolds numbers, and different spanwise and streamwise wavenumbers of the initial perturbation waves.

One of the issues surrounding computational studies of stability and transition involves the temporal versus spatial approach. Temporal models use a computational 'box' which travels with the phase speed of the T–S wave following a single wavelength of the disturbance as it evolves in time. This model permits periodicity in the streamwise direction, thus avoiding the outflow boundary condition problem and enables the use of available computer memory to resolve one wavelength. This issue is especially important for boundary-layer calculations where non-parallel effects, e.g. streamwise growth, are neglected in temporal studies. In channel flows, because the base flow remains parallel, there is less of a controversy and the temporal approach simply represents a different type of 'initial' condition. Consequently, for channel flows temporal models obtained good results for the simulation of transition into secondary instability and the breakdown stage (Orszag & Kells 1980; Kleiser 1982; Orszag & Patera 1983; Biringen 1984, 1987, 1990; Kleiser & Schumann 1984; May & Kleiser 1985; Zang & Hussaini 1985; Krist & Zang 1987; Asai & Nishioka 1989). However, in experiments on forced transition, disturbances are generated by a vibrating ribbon which exhibits spatial instability, and therefore spatial simulations offer direct comparisons between computations and experiments (Fasel 1989). The effects of temporal versus spatial computational models on the simulation of secondary instability in channel flows have not been documented to date. Although two-dimensional spatial simulations have been performed previously (Fasel & Bestek 1980; Patera 1984), to our knowledge the present work is the first spatial simulation of secondary instability in plane channel flow.

The present computational study involves an investigation of the differences between H- and K-type secondary instability in plane channel flow using a spatial mathematical model. To instigate the two types of instability, a wave triad generated from the spatial solutions of the Orr–Sommerfeld equation is imposed at the inflow boundary. Comparisons are made between the evolutionary characteristics of the two types of instability, and differences and agreements between the present spatial simulations and previous temporal simulations are documented. The effects of random initial conditions on the spatial development of secondary instability in plane channel flow will be the subject of a subsequent paper.

2. Computational procedure

The present numerical model integrates the three-dimensional, time-dependent, incompressible Navier–Stokes equations and the continuity equation for the perturbation quantities. These equations are non-dimensionalized by the channel half height, h, and the centreline velocity, U_c:

$$\frac{\partial u'_j}{\partial t} + u'_i \frac{\partial u'_j}{\partial x_i} + U_b \frac{\partial u'_j}{\partial x_1} + u'_2 \frac{\partial U_b}{\partial x_2} \delta_{j1} = -\frac{\partial p'}{\partial x_j} + \frac{1}{Re} \frac{\partial^2 u'_j}{\partial x_i \partial x_i}, \tag{1}$$

$$\frac{\partial u'_j}{\partial x_j} = 0. \tag{2}$$

In (1) and (2), $u'_j = (u', v', w')$ represents the perturbation velocity components in the streamwise (x), normal (y), and spanwise (z) directions, respectively (figure 1). The Reynolds number, Re, is defined as $Re = U_c h/\nu$, where ν is the kinematic viscosity. The perturbation pressure is given as p', δ_{jk} is the Kronecker delta, t is time, and U_b is the base (laminar) velocity profile defined as

$$U_b(u, v, w) = (1 - y^2, 0, 0). \tag{3}$$

At the channel walls the no-slip boundary conditions are imposed so that

$$u'_j(x, y = \pm 1, z, t) = 0, \tag{4}$$

and the inflow conditions are

$$\begin{aligned} u'_j(x = 0, y, z, t) &= A_{2d} \operatorname{Re}[(u'_{e2d}(y))_j \mathrm{e}^{-\mathrm{i}\omega_{r2d} t}] \\ &\quad + \tfrac{1}{2} A_{3d} \operatorname{Re}[(u'^{+}_{e3d}(y))_j \mathrm{e}^{\mathrm{i}(\beta z - \omega_{r3d} t)}] + \tfrac{1}{2} A_{3d} \operatorname{Re}[(u'^{-}_{e3d}(y))_j \mathrm{e}^{\mathrm{i}(\beta z - \omega_{r3d} t)}]. \end{aligned} \tag{5}$$

In (5), A_{2d} is the amplitude of the two-dimensional perturbation wave and A_{3d} is the total amplitude of the three-dimensional oblique wave pair. The complex spatial eigenfunctions, $(u'_{e2d})_j$ and $(u'_{e3d})_j$, are calculated by solving the Orr–Sommerfeld equation using the companion matrix method for a given Reynolds number, real spanwise wavenumber, β, and for the real frequencies of the two- and three-dimensional waves, ω_{2rd} and ω_{3rd}, respectively (Danabasoglu & Biringen 1990). The eigenfunctions are normalized such that the maximum amplitude of the streamwise component is unity with a zero phase shift. Superscripts + and − represent the eigenvectors calculated for $\beta > 0$ and $\beta < 0$, respectively. When $\omega_{r3d} = \omega_{r2d}$, the three-

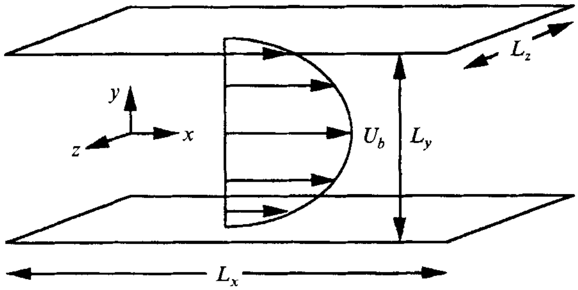

FIGURE 1. Schematic of the three-dimensional channel flow geometry.

dimensional disturbance field evolves into K-type instability and when $\omega_{r3d} = \frac{1}{2}\omega_{r2d}$, H-type instability develops. Also, $\mathrm{i} = \sqrt{-1}$ and Re indicates the real part of a complex number.

The Navier–Stokes equations are numerically integrated by a time-splitting procedure which uses the implicit Crank–Nicolson method on the normal diffusion terms and the explicit Adams–Bashforth method on the remaining terms. The equations are discretized in space on a non-staggered grid by fourth-order cental finite differences in the streamwise direction and by the Chebyshev collocation matrix method along the wall-normal direction. The assumption of periodicity in the spanwise direction allows the application of fast Fourier transforms. The pressure Poisson equation was solved by the capacitance matrix method (Kleiser & Schumann 1984; Streett & Hussaini 1986) which transforms the homogeneous Neumann problem into a non-homogeneous Dirichlet problem. The discretized Poisson equations were then integrated by the tensor product technique (Peltier, Biringen & Chait 1990; Huser & Biringen 1992) using matrix decomposition. At the outflow, boundary conditions were prescribed to ensure strictly outgoing waves. This was accomplished by appending a 'buffer domain' to the physical domain (the length of the buffer domain was about 30% of the physical domain) in which the governing equations were modified by reducing the streamwise viscous terms, the streamwise perturbation part of the convective velocity, and the right-hand side of the pressure Poisson equation to zero at the outflow boundary using a smooth coefficient function. Our previous numerical experiments have included rigorous testing of this technique demonstrating its suitability for use in both high- and low-amplitude wave propagation problems (Streett & Macaraeg 1989; Danabasoglu, Biringen & Streett 1990, 1991). The numerical scheme requires about 9.3 s of CPU time per time step on the CRAY-2 at NASA Langley Research Center for a $509(x) \times 41(y) \times 32(z)$ grid. Further details of the numerical method and the computer code used in this study are given in Danabasoglu (1992).

3. Results and discussion

In the present study, the generation of inflow conditions was controlled through the variation of the parameters in equation (5). In particular, we examined the effects of four different sets of these conditions outlined in table 1 (denoted as cases I-K, I-H, II-K, and II-H, where H and K indicate H- and K-type initial conditions, respectively). In cases II-H and II-K, we prescribed higher amplitudes and a higher spanwise wavenumber for the inflow conditions than in cases I-H and I-K, matching more closely the initial conditions used by Zang & Hussaini (1985) in their temporal

Case	Re	A_{2d}	A_{3d}	ω_{r2d}	ω_{r3d}	β
I-K	5000	2%	0.15%	0.33698	0.33698	± 1
I-H	5000	2%	0.15%	0.33698	0.16849	± 1
II-K	5000	3%	0.2%	0.33698	0.33698	± 2
II-H	5000	3%	0.2%	0.33698	0.16849	± 2

TABLE 1. Parameters for cases studied.

Case	L_x	L_y	L_z	N_x	N_y	N_z	λ_x	λ_z
I-K	55	2	2π	401	41	33	5.5	2π
I-H	47.5	2	2π	346	41	33	5.5	2π
II-K	33	2	π	241	41	33	5.5	π
II-H	33	2	π	241	41	33	5.5	π

TABLE 2. Mesh resolution used in the calculations. L represents the non-dimensional physical domain length, N is the number of grid points, and λ is the wavelength in a given direction.

Case	α_{2d}	α_{3d}
I-K	1.17249+i0.012873	1.02570+i0.068456
I-H	1.17249+i0.012873	0.52293+i0.019645
II-K	1.17249+i0.012873	0.91984+i0.258357
II-H	1.17249+i0.012873	0.37243+i0.083078

TABLE 3. Spatial eigenvalues of the Orr–Sommerfeld equation for the parameters given in table 1. α_{2d} and α_{3d} are the streamwise wavenumbers of the two- and three-dimensional waves, respectively.

simulations. Zang & Hussaini (1985) performed their calculations at $Re = 5000$, $\beta = \pm 2$, $A_{2d} = 5\%$, and $A_{3d} = 0.1\%$. In comparison, in cases II-H and II-K, we prescribed $Re = 5000$, $\beta = \pm 2$, $A_{2d} = 3\%$, and $A_{3d} = 0.2\%$. The choice of the lower two-dimensional amplitude in the present simulations was due to the explosive growth of both types of instabilities over very short streamwise distances for amplitudes greater than $A_{2d} = 3\%$. In fact, at this Reynolds number, both forced and unforced experiments indicate that larger amplitudes are not required for secondary instability and the formation of vortical structures. In all of the present simulations, the values chosen for Re and ω_{2d} correspond to the experimental conditions of Nishioka *et al.* (1980, 1981). Previous studies (Danabasoglu *et al.* 1991) have demonstrated that the mesh resolutions of the present simulations (given in table 2) are sufficient for accurate simulations of secondary instability. The streamwise physical lengths were chosen to ensure grid-independent solutions for each configuration. The spatial eigenvalues of the two- and three-dimensional disturbances, α_{2d} and α_{3d}, obtained from the Orr–Sommerfeld equations are listed in table 3.

The time step (Δt) for the simulations was assigned by trial and error by dividing one T–S period into 1000 parts to ensure numerical stability and time accuracy. Comparison of results for several test cases using smaller time steps proved the solutions to be independent of this time step. Upon convergence of the solutions, the instantaneous quantities were evaluated at the same phase position of the two-dimensional disturbance in time (either at T or $\frac{1}{2}T$, where T is the period of the T–S wave) for both H- and K-type instability calculations.

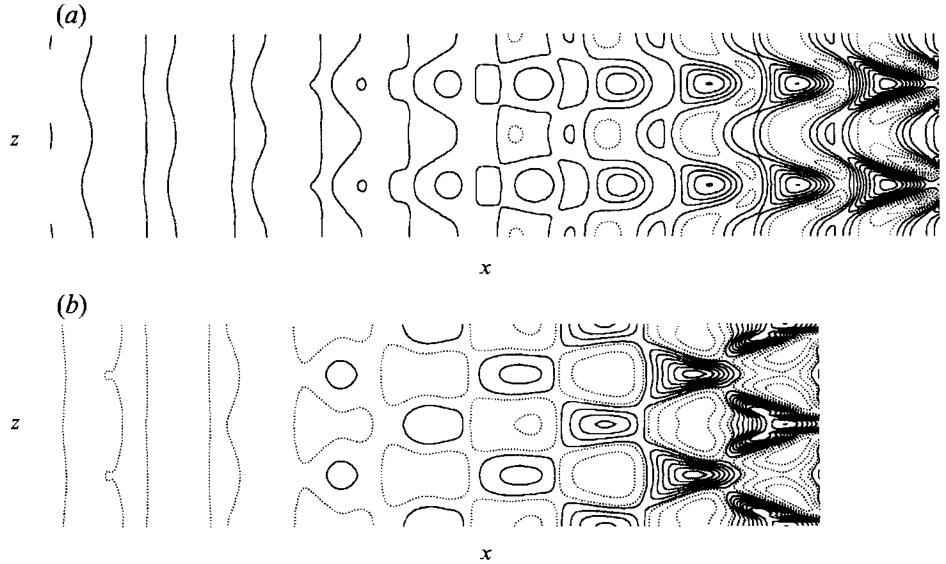

FIGURE 2. Contours of ω_z' in the (x, z)-plane near the critical layer, $y \approx 0.85$. (*a*) Case I-K: contour levels range from -0.45 to 0.3, $L_x = 55$; (*b*) Case I-H: contour levels range from -0.95 to 0.4, $L_x = 47.5$. The flow direction is from left to right and the spanwise length of the domain is doubled to clearly depict the pattern of Λ-vortices. Solid and dashed contours denote negative and positive levels, respectively.

3.1. *Development of vortical structures and the high-shear layer*

In this section we examine the spatial development of the Λ-vortices and the high-shear layer for both H- and K-type instabilities. The discussion presented in §§3.1–3.4 is confined to cases I-H and I-K; the effects of higher initial amplitudes and larger spanwise wavenumbers (cases II-H and II-K) are considered in §3.5.

In figures 2(*a*) and 2(*b*), spanwise perturbation vorticity (ω_z') contours in the (x, z)-plane close to the critical layer ($y \approx 0.85$) are displayed. For both types of instability these contours reveal the streamwise evolution of the Λ-vortices. The spanwise length of the domain in these figures has been increased to $2\lambda_z$ in order to clearly depict the Λ-vortex patterns. The distinctive Λ-shaped footprints can clearly be discerned in the characteristic peak–valley splitting (non-staggered pattern) for K-type instability (figure 2*a*) and the staggered pattern of the vortices is manifested in figure 2(*b*) for H-type instability. The growth of H-type instability occurs over a shorter distance and attains higher amplitudes than the K-type at comparable x-locations. These results are in accordance with previous theoretical studies (Herbert 1983*a*, *b*) and temporal simulations (Spalart & Yang 1987 – boundary layers; Singer *et al.* 1987, 1989 – channel flows) in which random three-dimensional disturbances and two-dimensional eigenfunctions were prescribed as initial conditions allowing the competition of H- and K-type modes. Accordingly, low-amplitude two-dimensional disturbances lead to the dominance of H-type instability while higher amplitudes lead to the dominance of K-type instability. However, in contrast to the present results, previous temporal computations (Zang & Hussaini 1985; Krist & Zang 1987; Laurien & Kleiser 1989) on forced H- and K-type secondary instability using initial conditions of the type given by equation (5) indicate stronger K-type growth regardless of the initial amplitude and spanwise wavenumber.

In figures 3(*a*)(i) and 3(*b*)(i), instantaneous $(U_b + u')$ velocity profiles are plotted over

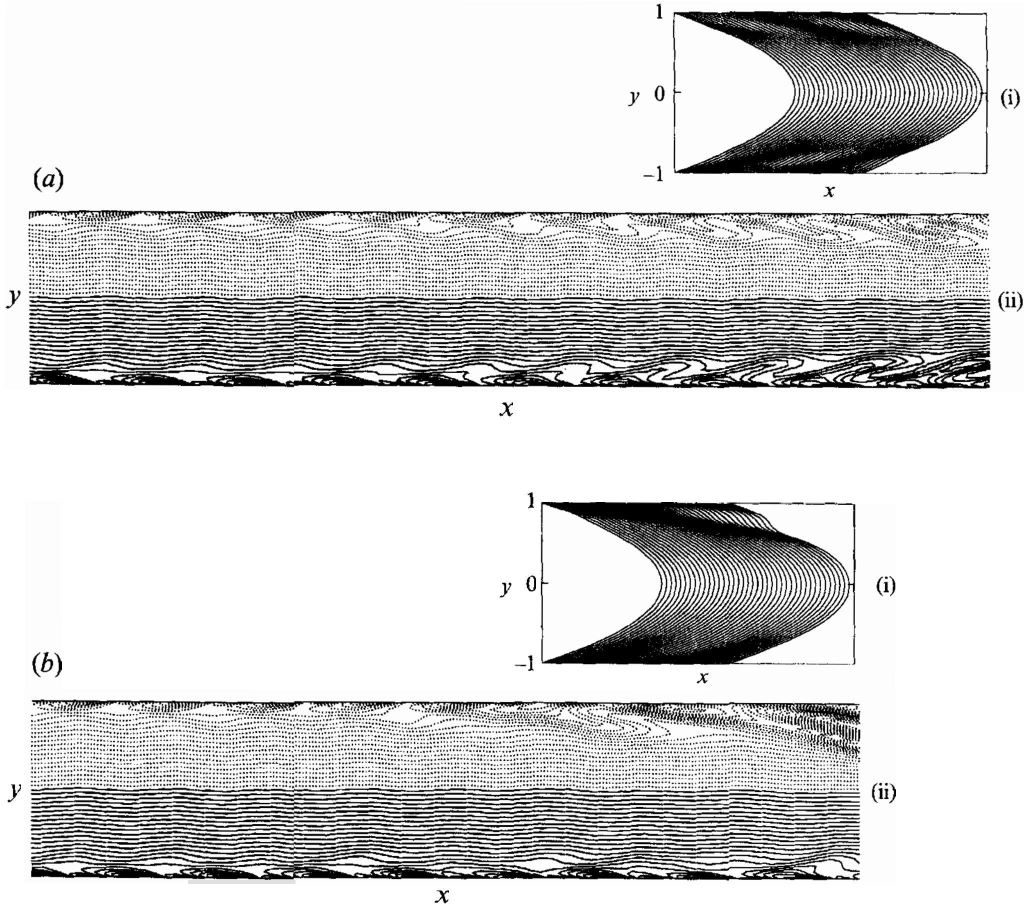

FIGURE 3. (*a*) Case I-K: (i) instantaneous velocity profiles, $z = 0.5\lambda_z$; (ii) contours of ω_z in the (x, y)-plane, $z = 0.5\lambda_z$. (*b*) Case I-H: (i) instantaneous velocity profiles, $z = \lambda_z$; (ii) contours of ω_z in the (x, y)-plane, $z = \lambda_z$. The direction of the flow is from left to right. The instantaneous profiles are plotted over the last two T–S wavelengths. Contour levels range from -2.6 to 2.6, and solid and dashed contours denote negative and positive levels, respectively.

the last two T–S wavelengths of the physical domain; the z-locations of these profiles correspond to the peak plane, $z = 0.5\lambda_z$, for K-type instability and $z = \lambda_z$ for H-type instability (of course, the definition of the terms 'peak plane' and 'valley plane' are not applicable to H-type instability). For K-type instability, the strong inflexions contained in these distributions (figure 3*a*i) demonstrate the formation of local high-shear layers around $y = \pm 0.6$, in agreement with the experiments of Nishioka *et al.* (1980) and with previous temporal computations. At the valley plane ($z = \lambda_z$), the intensity of the inflexions diminish and there is no evidence of a high-shear layer. The profiles for H-type instability (figure 3*b*i) reveal several differences in comparison with the K-type. First, the intensity of the high-shear layer (developing at $y = +0.6$) and the profile inflexions at the upper wall are greater than at the lower wall, i.e. the evolution of the disturbances is biased toward the upper wall. Second, the shear layer at the upper wall extends over the entire two T–S wavelengths in accordance with the generation of a subharmonic. Finally, due to the staggered arrangement of the Λ-vortices in H-type instability, strong shear layers exist at spanwise positions other than $z = \lambda_z$. The strong inflexions exhibited by the instantaneous velocity profiles in H-type instability were accompanied by strongly distorted signals in the time history of u', suggesting the occurrence of the incipient spike stage. In K-type instability, the u' signals were only marginally distorted from their initial sinusoidal signature, indicating that H-type instability undergoes an earlier breakdown process than the K-type.

The development of the high-shear layers can also be observed from an examination of the contour plots of total spanwise vorticity, ω_z, at the same spanwise positions as in figures 3(*a*)(i) and 3(*b*)(i). For K-type instability (figure 3*a*ii), the evolution of the shear layer occurs mainly at the peak plane in a manner consistent with previous temporal simulations and experimental results. Because of the antisymmetric inflow conditions about $y = 0$, the structures appearing on the upper and lower walls are 180° out of phase with each other. In the upstream region of the channel, the contours of ω_z for H-type instability (figure 3*b*ii) are also influenced by this antisymmetry, but the vortical structures undergo a sudden intensification and stretching in the vicinity of the upper wall. This biased evolution of H-type secondary instability is in accordance with Herbert's secondary instability theory (1983*a*) and was also captured in the temporal channel flow simulations of May & Kleiser (1985). Their work demonstrated that at low spanwise wavenumbers (β) disturbances oscillate between the two walls, while at high β-values transition takes place on only one wall.

3.2. *Statistical analysis and mean flow field structures*

Streamwise and normal root-mean-square (r.m.s.) distributions are presented in figures 4–9. Because the present simulations are spatial, the r.m.s. values are true time averages defined as

$$u'_{rms} = \left(\frac{1}{N_t}\sum_t (u' - u'_m)^2\right)^{\frac{1}{2}}, \tag{6}$$

where N_t is the number of time steps in one T–S period (or two T–S periods for the H-type case) and u'_m is the mean velocity,

$$u'_m = \frac{1}{N_t}\sum_t u'. \tag{7}$$

We also evaluated the shear-stress, $\overline{u'v'}$, as

$$\overline{u'v'} = \frac{1}{N_t}\sum_t (u' - u'_m)(v' - v'_m). \tag{8}$$

The streamwise distributions of $(u'_{rms})_{max}$ and $(v'_{rms})_{max}$ (maximum over y) at $z = 0.5\lambda_z$ are presented in figures 4(*a*) and 4(*b*); owing to the spanwise antisymmetry of the w' inflow conditions, $(w'_{rms})_{max}$ at $z = 0.5\lambda_z$ is zero. For K-type instability (figure 4*a*), $(v'_{rms})_{max}$ gradually decays while $(u'_{rms})_{max}$ increases to about one and a half times its original amplitude. In comparison, the $(u'_{rms})_{max}$ distribution for H-type instability (figure 4*b*) exhibits the same behaviour, but attains amplitudes about three times higher than those of K-type, indicating that breakdown occurs faster in the H-type disturbance environment. The r.m.s. variations at a plane where w' is maximum ($z = 0.25\lambda_z$) are plotted in figures 5(*a*) and 5(*b*). Accordingly, for both types of instability, $(u'_{rms})_{max}$ decays until the rapidly growing $(w'_{rms})_{max}$ component reaches comparable amplitudes; beyond this point, $(u'_{rms})_{max}$ begins to increase.

The variation of the r.m.s. velocity components as a function of the wall-normal direction are shown in figures 6–9 for different streamwise locations. The spanwise

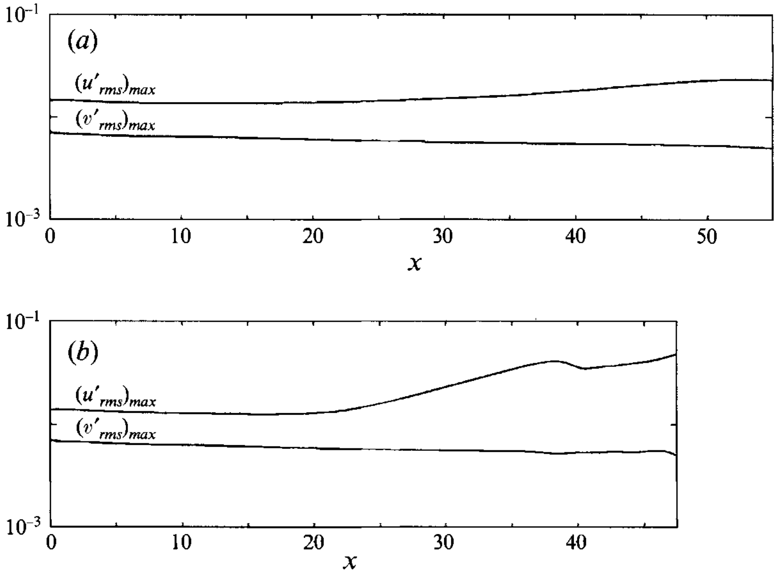

FIGURE 4. Streamwise distributions of $(u'_{rms})_{max}$ and $(v'_{rms})_{max}$ at $z = 0.5\lambda_z$ (maximum over y). (*a*) Case I-K; (*b*) Case I-H.

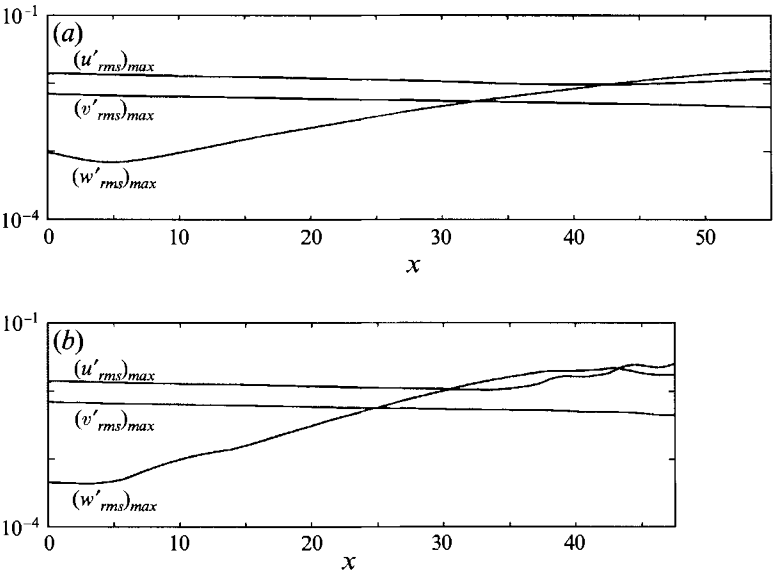

FIGURE 5. Streamwise distributions of $(u'_{rms})_{max}$, $(v'_{rms})_{max}$ and $(w'_{rms})_{max}$ at $z = 0.25\lambda_z$ (maximum over y). (*a*) Case I-K; (*b*) Case I-H.

coordinates correspond to $z = 0.5\lambda_z$ for the u'_{rms} and v'_{rms} distributions; the distributions of w'_{rms} were obtained at $z = 0.25\lambda_z$. For K-type instability (figure 6*a*), the local maxima of the u'_{rms} profiles increase and their y-locations move toward the channel centre as the flow develops downstream. This behaviour may be associated with the outward diffusion of spanwise vorticity from the wall due to the motion induced by the streamwise vortices, thus resulting in the formation of the high-shear layer (Tani 1969). The same type of behaviour is seen at the upper wall for H-type

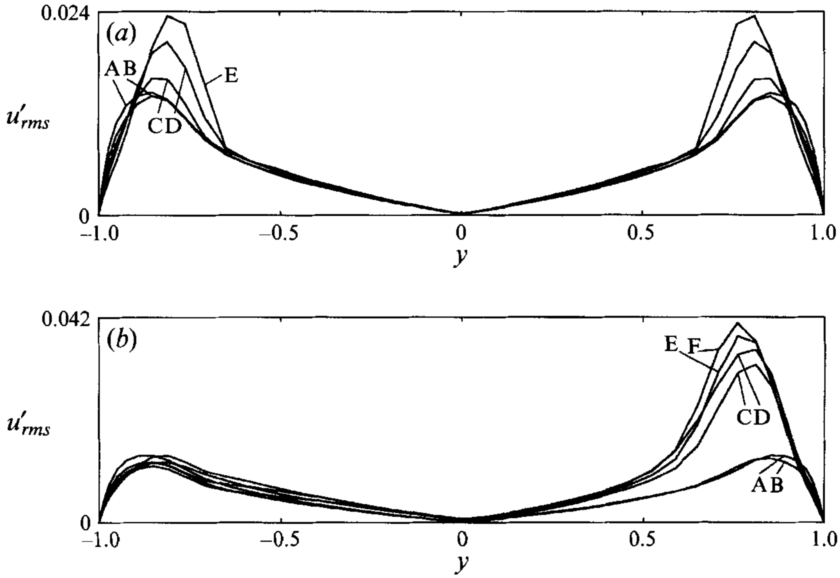

FIGURE 6. Normal distributions of u'_{rms} at $z = 0.5\lambda_z$. (*a*) Case I-K: A, $x = 2.61$; B, $x = 20.49$; C, $x = 34.24$; D, $x = 44.55$; and E, $x = 54.18$. (*b*) Case I-H: A, $x = 2.61$; B, $x = 20.49$; C, $x = 34.24$; D, $x = 41.11$; E, $x = 43.45$; and F, 45.24.

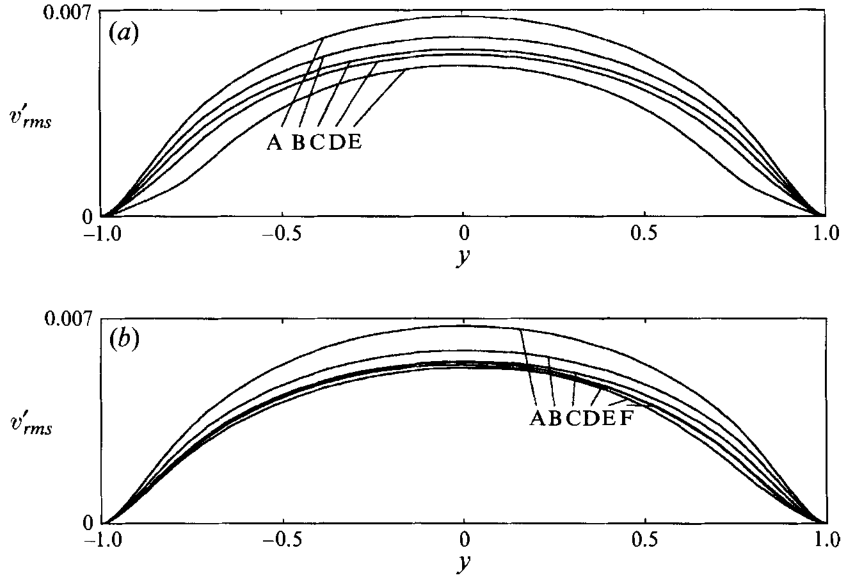

FIGURE 7. Normal distributions of v'_{rms} at $z = 0.5\lambda_z$. (*a*) Case I-K: A–E as in figure 6(*a*); (*b*) Case I-H: A–F as in figure 6(*b*).

instability (figure 6*b*), while at the lower wall there is little growth in the u'_{rms} amplitudes. For both K- and H-type instability, the distributions in figures 7(*a*) and 7(*b*) indicate a decrease in $(v'_{rms})_{max}$ in the streamwise direction. Downstream, the profiles become inflexional, revealing increasing gradients near the walls. Distributions of w'_{rms} are similar to those of u'_{rms}: in K-type instability, $(w'_{rms})_{max}$ increases with x at both walls (figure 8*a*), and in H-type instability, this increase takes place only at

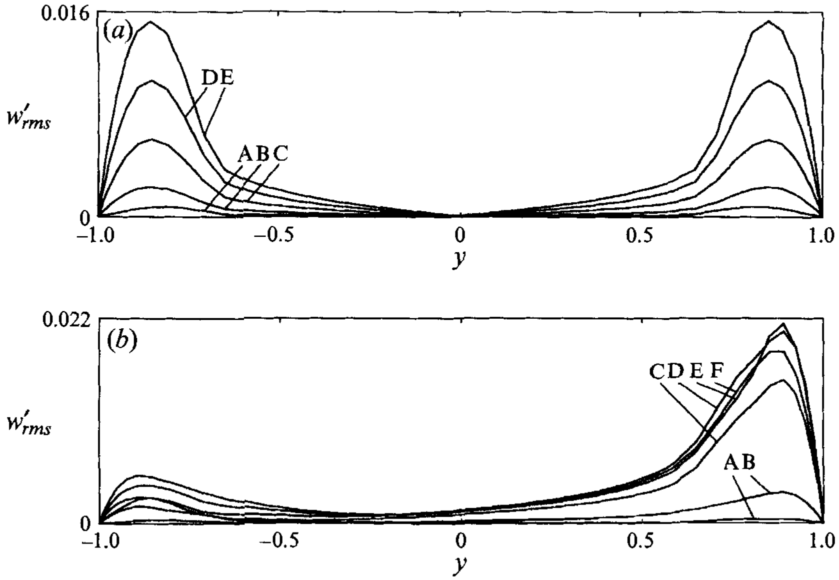

FIGURE 8. Normal distributions of w'_{rms} at $z = 0.25\lambda_z$. (*a*) Case I-K: A–E as in figure 6(*a*); (*b*) Case I-H: A–F as in figure 6(*b*).

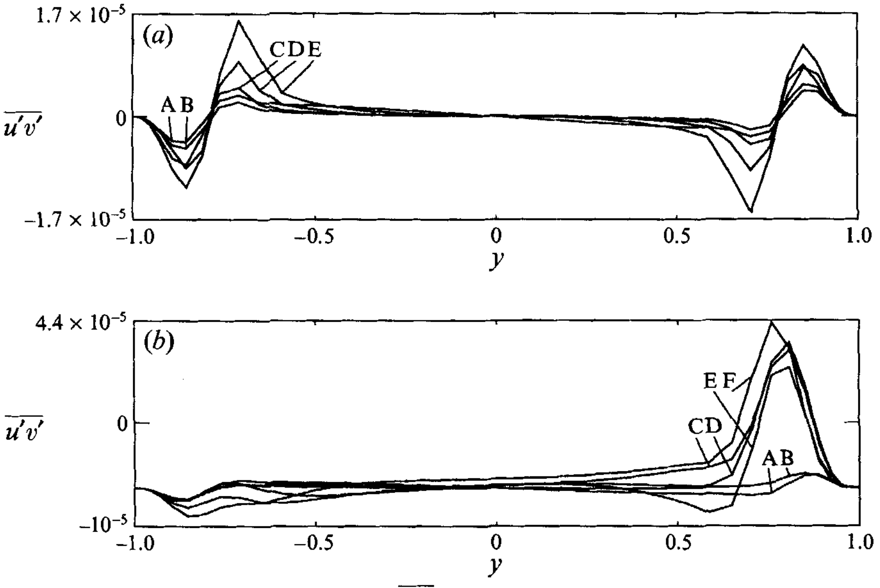

FIGURE 9. Normal distributions of $\overline{u'v'}$ at $z = 0.5\lambda_z$. (*a*) Case I-K: A–E as in figure 6(*a*); (*b*) Case I-H: A–F as in figure 6(*b*).

the upper wall. The locations of $(w'_{rms})_{max}$, however, remain almost invariant which supports the idea that it is the spanwise vorticity that is diffused from the wall region, i.e. the high-shear layer consists mainly of spanwise vorticity. The normal distributions of the shear stress, $(\overline{u'v'})$, at $z = 0.5\lambda_z$ are presented in figures 9(*a*) and 9(*b*). As expected, owing to the transfer of energy from the mean flow to the fluctuating flow, maximum amplitudes for this quantity also increase with x. For H-type instability, the amplitude increase takes place only at the upper wall, while at the lower wall the amplitudes remain relatively constant indicating that the main energy transfer in

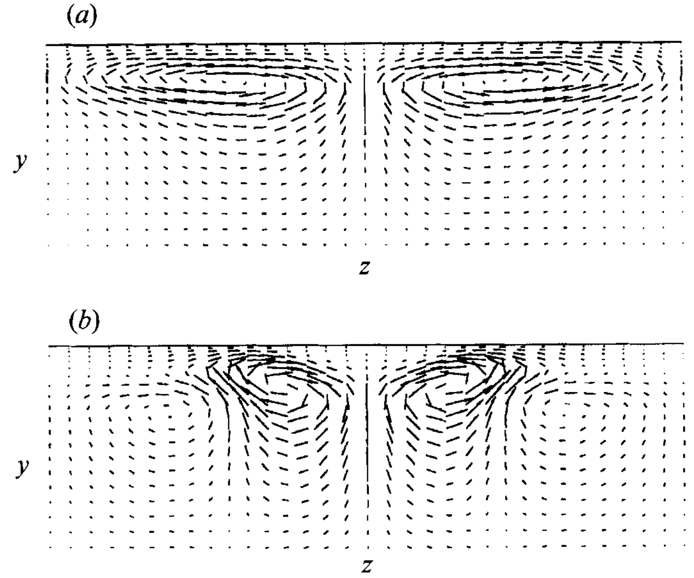

FIGURE 10. Velocity vectors of the secondary mean flow in the upper half of the channel. Case I-K: (a) $x = 27.5$, vector magnitudes are multiplied by 400; (b) $x = 55.0$, vector magnitudes are multiplied by 50. The direction of the flow is out of the plane of the paper.

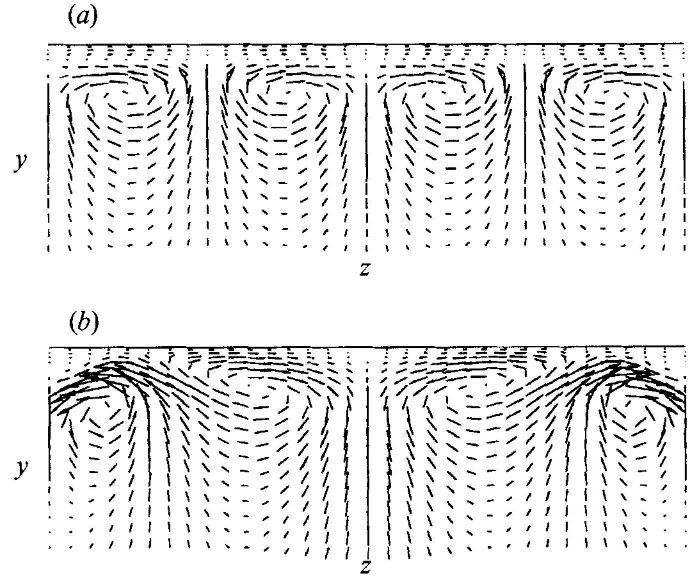

FIGURE 11. Velocity vectors of the secondary mean flow in the upper half of the channel. Case I-H: (a) $x = 27.5$, vector magnitudes are multiplied by 800; (b) $= 44.69$, vector magnitudes are multiplied by 50. The direction of the flow is out of the plane of the paper.

H-type instability is occurring at the upper wall. In rough correspondence with the u'_{rms} distributions, the local maxima of $\overline{u'v'}$ move toward the channel centre in agreement with temporal simulations (Biringen 1984).

The mean secondary flow velocity vectors in several (y, z)-planes are plotted in figures 10 and 11. For K-type instability, the doubling of the vortex cells in the downstream region at $x = 55$ is the result of energy transfer to the first spanwise

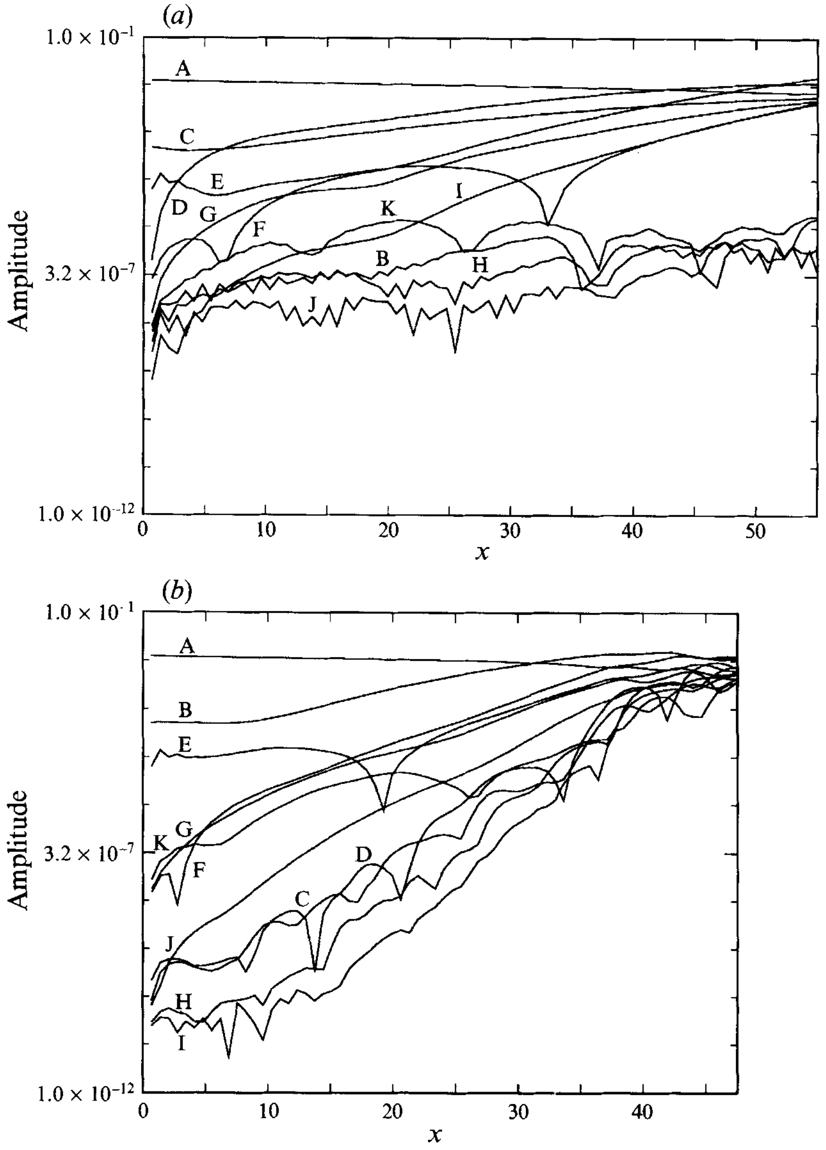

FIGURE 12. Streamwise distributions of Fourier amplitudes at $y \approx 0.85$. (*a*) Case I-K; (*b*) Case I-H. A, $(\omega, 0)$; B, $(\frac{1}{2}\omega, \beta)$; C, (ω, β); D, $(0, \beta)$; E, $(0, 0)$; F, $(0, 2\beta)$; G, $(\omega, 2\beta)$; H, $(\frac{1}{2}\omega, 2\beta)$; I, $(\omega, 3\beta)$; J, $(\frac{1}{2}\omega, 3\beta)$; and K, $(\frac{1}{2}\omega, 0)$.

harmonic, i.e. $\beta = 2$ (figure 10*b*). Two vortex pairs appear initially in H-type instability due to the inflow conditions (figure 11*a*), and as the flow develops downstream, the nonlinear interaction of the oblique waves intensifies the vortex cells (figure 11*b*).

3.3. *Spectral analysis*

The streamwise variation of the u' Fourier amplitudes are presented in figures 12(*a*) and 12(*b*). The u'-velocity was recorded for two periods of the T–S wave in time at $y \approx 0.85$, and the signals were Fourier transformed in time and in z. Here, we denote a mode in the frequency/wavenumber space as a wavevector, $\boldsymbol{k} = (m\omega, n\beta)$, where ω is the T–S frequency and β is the spanwise wavenumber; consequently, for the modes defined below, $m = 0, \frac{1}{2}, 1$ and $n = 0, 1, 2, 3$. The amplitude distributions were obtained for the primary two-dimensional mode $\boldsymbol{k} = (\omega, 0)$, the fundamental mode $\boldsymbol{k} = (\omega, \beta)$, the subharmonic mode $\boldsymbol{k} = (\frac{1}{2}\omega, \beta)$, the spanwise mode $\boldsymbol{k} = (0, \beta)$, the mean perturbation mode $\boldsymbol{k} = (0, 0)$, the spanwise harmonic modes $(0, 2\beta)$, $(\omega, 2\beta)$, $(\frac{1}{2}\omega, 2\beta)$, $(\omega, 3\beta)$ and $(\frac{1}{2}\omega, 3\beta)$, and the subharmonic two-dimensional mode $(\frac{1}{2}\omega, 0)$. The results of this analysis for K-type instability (figure 12*a*) indicate that the primary mode ($(\omega, 0)$; curve A) decays slowly while the fundamental mode ((ω, β); curve C) grows steadily with increasing x. Downstream, the $(0, \beta)$ mode (curve D) shows rapid growth and its amplitude exceeds both the primary and fundamental modes. The appearance of the $(0, \beta)$ mode in K-type instability is an important part of secondary instability theory (Herbert 1983*a*, *b*), and because it is not included in the present initial conditions, it has to appear due to the nonlinear interaction of the three-dimensional wave pair with the two-dimensional wave before secondary instability develops. Zang & Hussaini (1985) found that suppression of the $(0, \beta)$ mode in their forced K-type temporal instability simulations stabilized the growth of the (ω, β) mode, and several other studies revealed that the strong growth of the $(0, \beta)$ mode (Kim & Moser 1989) or augmentation of the $(0, \beta)$ amplitude (by the addition of streamwise vortices as in Singer *et al.* 1987, 1989 and Konzelmann, Rist & Fasel 1989) will bias the flow towards K-type instability. The amplitude of the first spanwise harmonic mode ($(0, 2\beta)$; curve F) exhibits a large amplitude increase in accordance with the vortex doubling observed in figure 10(*b*). Figure 12(*a*) also indicates the existence of latent subharmonic modes ($\boldsymbol{k} = (\frac{1}{2}\omega, \beta)$, $(\frac{1}{2}\omega, 2\beta)$, $(\frac{1}{2}\omega, 3\beta)$, $(\frac{1}{2}\omega, 0)$; curves B, H, J, and K) whose amplitudes are relatively lower than the other modes. The subharmonic modes are energized by the interaction of the three-dimensional modes with the $(\frac{1}{2}\omega, 0)$ mode which obtains its energy directly from the mean mode (see §3.4). The streamwise distribution of the mean perturbation mode ($(0, 0)$; curve E) for K-type instability demonstrates a sudden dip at $x \approx 33$. Downstream of this point, the $(0, 0)$ amplitude increases and reaches magnitudes comparable to the other modes. The $(0, 0)$ mode also exhibits similar behaviour for H-type instability (figure 12*b*), but this dip occurs at a location further upstream than in K-type instability at $x \approx 19.25$. As we will explain later, for both H- and K-type instabilities this dip indicates a change in the energy transfer to and from the $(0, 0)$ mode.

The subharmonic mode ($(\frac{1}{2}\omega, \beta)$; curve B in figure 12*b*) in H-type instability follows the same trend as the fundamental mode (ω, β) in K-type instability, displaying a steady rise in its amplitude. Once the dominant $(\frac{1}{2}\omega, \beta)$ amplitude exceeds the $(\omega, 0)$ amplitude (curve A), the $(\omega, 0)$ mode begins to oscillate in a manner typically observed during the spike stage. The (ω, β) and $(0, \beta)$ modes (curves C and D) exhibit relatively strong growth in the H-type case. The growth of the $(0, \beta)$ mode in H-type instability is contrary to the temporal channel simulations of Zang & Hussaini (1985) and Krist & Zang (1987) where no contribution from the $(0, \beta)$ mode is indicated. Given the modes that exist in the inflow conditions for the H-type instability simulation, i.e. the $(\frac{1}{2}\omega, \pm\beta)$, $(\omega, 0)$, and $(0, 0)$ modes, it is not likely that the $(0, \beta)$ mode (or the (ω, β) mode) will develop through the nonlinear interactions of these waves. However, it is interesting to note that the two-dimensional subharmonic mode ($(\frac{1}{2}\omega, 0)$, curve K) has substantial amplitude throughout the domain, and interacts with the subharmonic oblique wave pair to produce both the $(0, \beta)$ and (ω, β) modes. As will be demonstrated in the subsequent section, the appearance of the $(\frac{1}{2}\omega, 0)$ mode in both H- and K-type instability from numerical noise is due to direct energy transfer from the mean mode.

In both types of secondary instability, several three-dimensional modes acquire high amplitudes near the inflow boundary and continue to grow downstream. In particular, the $(0, 2\beta)$ and $(\omega, 2\beta)$ modes (curves F and G in figure 12) in H- and K-type instability are prevalent, and the $(\omega, 3\beta)$ mode in K-type (curve I in figure 12*a*) and the $(\frac{1}{2}\omega, 3\beta)$ mode in H-type instability (curve J in figure 12*b*) also obtain relatively high amplitudes. The existence of large-amplitude $(0, 2\beta)$ and $(\omega, 2\beta)$ modes for K-type instability is caused by energy transfer from the $(0, \beta)$ and (ω, β) modes which have initially large amplitudes. For H-type instability, the $(0, 2\beta)$ and $(\omega, 2\beta)$ modes are excited nonlinearly when the oblique waves (initial conditions) reach sufficient amplitude to interact. Each of the higher harmonics of (ω, β) for K-type instability grow gradually as the flow evolves downstream, thus indicating a smooth spreading of energy into the wavenumber spectrum. In contrast, in H-type instability the amplitudes of the higher wavenumbers, $(\frac{1}{2}\omega, n\beta)$, increase in a very different manner. There is a sudden 'burst' in the energy of these modes in accordance with the volatile nature observed in the H-type instability simulation.

3.4. *Nonlinear energy transfer*

The transfer of energy between various modes is also a useful tool to aid in the understanding of secondary instability mechanisms. Previous theoretical work (Croswell 1985) and temporal simulations (Orszag & Patera 1983; Singer *et al.* 1987) have demonstrated that during secondary instability, for both H- and K-types, the transfer of energy is mainly from the (0, 0) mode to the three-dimensional modes, (ω, β) and $(\frac{1}{2}\omega, \beta)$. The three-dimensional modes then transfer energy into the two-dimensional mode $(\omega, 0)$, and the two-dimensional wave mediates the energy transfer between the mean and three-dimensional modes. This process establishes a self-sustaining energy feedback loop for secondary instability (Herbert 1988).

For the present spatial simulations, the intermodal energy transfer mechanisms were examined by determining the local nonlinear energy transfer within a wave triad, i.e. between three modes, $\boldsymbol{k}$, $\boldsymbol{k}'$, and $\boldsymbol{k}-\boldsymbol{k}'$, in a manner similar to Singer *et al.* (1987). The relation that expresses the spectral nonlinear energy transfer is derived from the momentum equation written for the total velocity,

$$\frac{\partial u_j}{\partial t}+u_i\frac{\partial u_j}{\partial x_i}=-\frac{\partial p}{\partial x_j}+\frac{1}{Re}\frac{\partial^2 u_j}{\partial x_i\,\partial x_i}. \tag{9}$$

Equation (9) is first transformed into the frequency–wavenumber, $\boldsymbol{k}=(m\omega, n\beta)$, Fourier space and then multiplied by the complex conjugate, $\hat{u}^{\dagger}(x, y, \boldsymbol{k})$, in order to form the energy equation. The nonlinear spectral energy transfer is then obtained from the convective term of the energy equation:

$$-\sum_i\sum_j \mathrm{Re}\,(\hat{u}_i(x,y,\boldsymbol{k}')\,\hat{u}_j^{\dagger}(x,y,\boldsymbol{k})\,\mathscr{L}_i(\hat{u}_j(x,y,\boldsymbol{k}-\boldsymbol{k}'))). \tag{10}$$

The derivation of the convection term in (10) differs from the temporal analysis of Singer *et al.* (1987) in that they transform the momentum equation into the Fourier wavenumber space, $\boldsymbol{k}=(m\alpha, n\beta)$, not the frequency–wavenumber space as in the present spatial analysis. Therefore, for the temporal case this equation represents the rate of nonlinear energy transfer, whereas for the present spatial problem, it represents spectral energy transfer to a given frequency. The derivative operator, L_i, in (10) is defined as

$$\mathscr{L}_1=\frac{\partial}{\partial x},\quad \mathscr{L}_2=\frac{\partial}{\partial y},\quad \mathscr{L}_3=\mathrm{i}k_z. \tag{11\,a–c}$$

In the present analysis, the effects of pressure on the spectral energy transfer were neglected, based upon the results of previous studies (Orszag & Patera 1983; Croswell

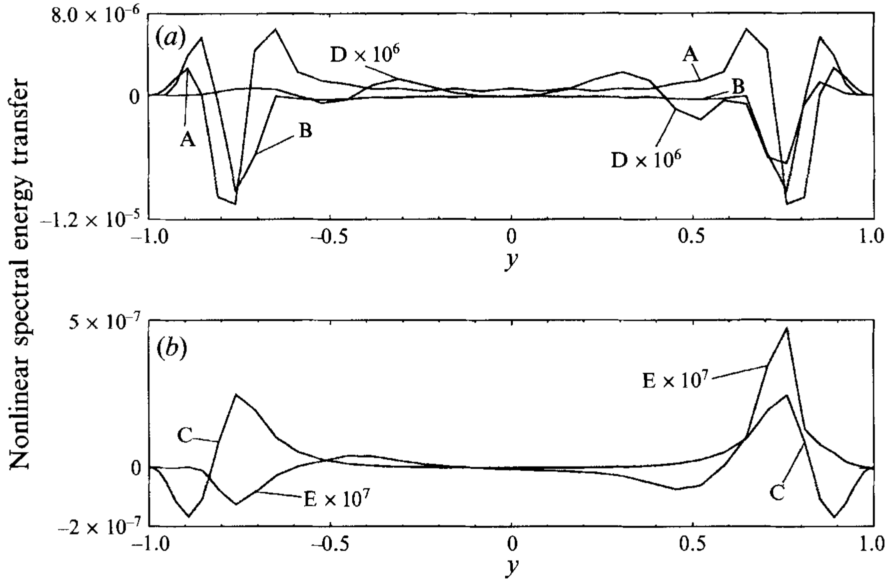

FIGURE 13. Normal distributions of nonlinear spectral energy transfer at $x = 49.36$. Case I-K: (*a*) A, B, and D as in table 4; (*b*) C and E as in table 4.

1985) which demonstrated that the integrated effect of perturbation pressure on intermodal energy transfer was zero. Singer *et al.* (1987) determined that in the early stages of their simulations, pressure was important in diffusing energy from the centre of the channel to the walls. However, this was a consequence of the initial conditions implemented in their simulations; the three-dimensional disturbances were initiated by 'centre modes', and in the later stages of their simulations, i.e. during the evolution of secondary instability, the pressure had a negligible effect on the nonlinear energy transfer rates.

Figures 13 and 14 contain the normal distributions of spectral energy transfer between different modes forming a wave triad (listed in table 4) at $x = 49.36$ and $x = 36.98$ for K- and H-type instability, respectively. Note that in these figures the positive portions of the distributions indicate energy transfer from $\boldsymbol{k}'$ and $\boldsymbol{k}-\boldsymbol{k}'$ to $\boldsymbol{k}$, while the negative portions correspond to energy transfer from $\boldsymbol{k}$ to $\boldsymbol{k}'$ and $\boldsymbol{k}-\boldsymbol{k}'$. Several investigators have normalized these quantities by a local scale based on the energy contained in wavenumbers $\boldsymbol{k}'$ and $\boldsymbol{k}-\boldsymbol{k}'$. While this may yield some useful information, it does not provide a direct quantitative comparison of energy transfer between different wave triads, i.e. comparisons between various sets of $\boldsymbol{k}$, $\boldsymbol{k}'$, and $\boldsymbol{k}-\boldsymbol{k}'$ could not be made unless a global normalization constant was used. Therefore, in the present work the spectral energy transfer terms were normalized by an arbitrary global scale. Examination of figures 13 and 14 reveals several aspects common to both H- and K-type instability. First, the highest energy transfer for each wave triad occurs in regions near the critical layer, $y \approx \pm 0.85$. In H-type instability, the distributions of the energy transfer are mostly biased towards the upper wall, while in K-type instability, the distributions are mostly symmetric with respect to $y = 0$. In figures 13(*b*) and 14(*b*) there is a net energy transfer from the three-dimensional waves to the two-dimensional wave (sets C and E in table 4). It is interesting to note that in H-type instability (figure 14*b*), the energy transfer between the two-dimensional wave and the fundamental modes (curve C) takes place at both walls, but the net effect of this activity at the lower

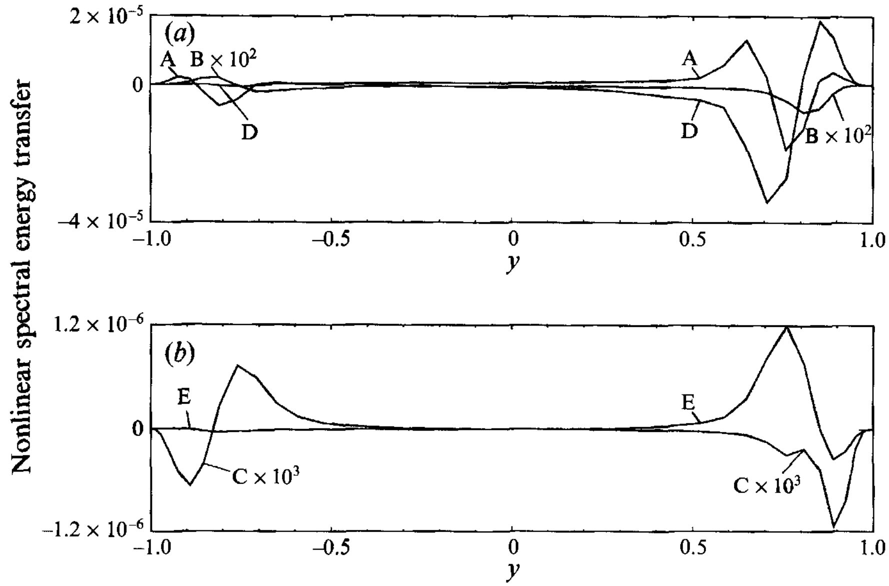

FIGURE 14. Normal distributions of nonlinear spectral energy transfer at $x = 36.98$. Case I-H: (*a*) A, B, and D as in table 4; (*b*) C and E as in table 4.

Set	$\boldsymbol{k}$	$\boldsymbol{k}'$	$\boldsymbol{k}-\boldsymbol{k}'$
A	$(0,0)$	$(\omega,0)$	$(-\omega,0)$
B	$(0,0)$	(ω,β)	$(-\omega,-\beta)$
C	$(\omega,0)$	(ω,β)	$(0,-\beta)$
D	$(0,0)$	$(\frac{1}{2}\omega,\beta)$	$(-\frac{1}{2}\omega,-\beta)$
E	$(\omega,0)$	$(\frac{1}{2}\omega,\beta)$	$(\frac{1}{2}\omega,-\beta)$

TABLE 4. Wave triads examined in the nonlinear spectral energy transfer analysis ($\omega = 0.33698$ and $\beta = 1$).

wall is almost zero. At the upper wall, the distributions indicate transfer mainly to the fundamental three-dimensional modes from the two-dimensional mode. However, more energy is being fed to the two-dimensional mode from the subharmonic modes (curve E) than the energy lost to the fundamental. Hence, there is a net energy gain by the two-dimensional mode. Also, as expected the prevalent three-dimensional modes, i.e. the $\boldsymbol{k} = (\frac{1}{2}\omega, \beta)$ mode in H-type instability (curves D and E in figure 14) and the $\boldsymbol{k} = (\omega, \beta)$ mode in K-type instability (curves B and C in figure 13), predominantly receive and transfer more energy than any of the other three-dimensional modes. The energy transfer between the mean and three-dimensional modes in H-type instability reaches higher amplitudes than those in the K-type indicating the stronger nature of H-type instability. These observations are generally in accordance with previous temporal studies (Orszag & Patera 1983; Croswell 1985; Singer *et al.* 1987).

Figures 15(*a*) and 15(*b*) display streamwise distributions of the maximum intermodal spectral energy transfer. Initially, in both H- and K-type instability, the dominant energy transfer occurs between the mean and the two-dimensional mode and the energy transfer decreases slowly as the flow develops downstream (the solid and dotted lines for Set A in figure 15*a*, *b*). The x-locations where the energy transfer between the

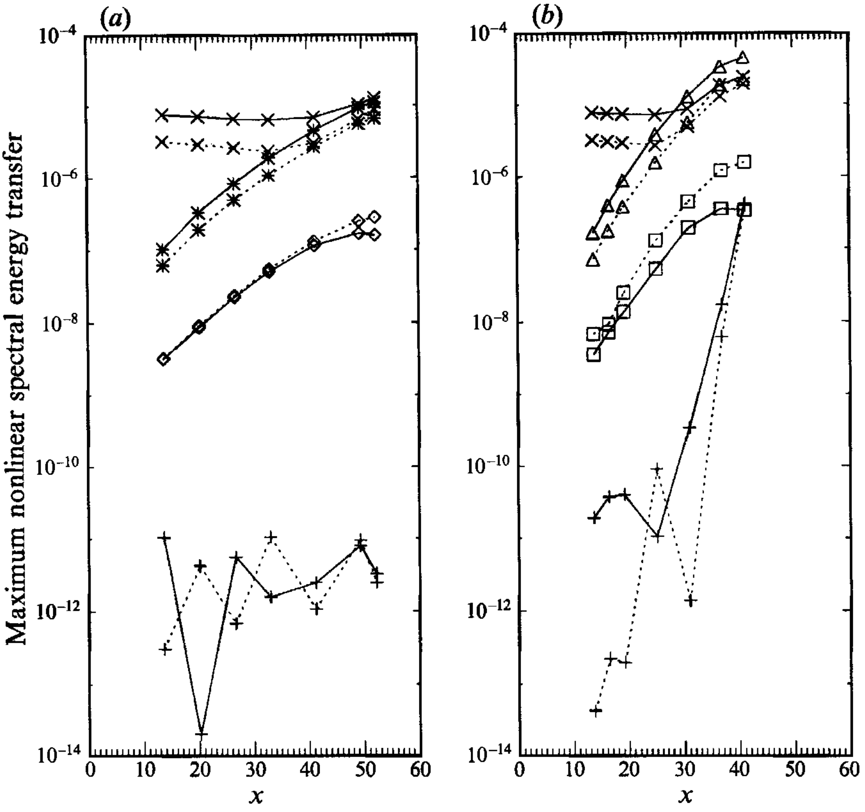

FIGURE 15. Streamwise distributions of maximum nonlinear spectral energy transfer. (*a*) Case I-K; (*b*) Case I-H. Dotted lines denote energy transfer from k' and $k-k'$ to k, and solid lines denote energy transfer from k to k' and $k-k'$. Sets A–E are defined in table 4. ×, Set A; *, Set B; ◇, Set C; △, Set D; □, Set E; +, $k = (0,0)$, $k' = (\frac{1}{2}\omega, 0)$, and $k-k' = (-\frac{1}{2}\omega, 0)$.

mean and the two-dimensional mode reaches a minimum closely correspond to the dip observed in the amplitude of the perturbation mean mode (curve E in figure 12*a*, *b*). The transfer of energy between the three-dimensional modes and the (0, 0) mode (the dotted and solid lines for Sets B and D in figure 15*a*, *b* respectively), continuously increases and in fact, for H-type instability the energy transfer to the subharmonic modes exceeds that from the mean mode to the two-dimensional mode, implying the inception of the spike stage. Also, this analysis demonstrates that as the flow develops downstream, there is a net energy transfer from the three-dimensional modes to the two-dimensional mode as indicated by the dotted and solid lines for Sets C and E in figure 15(*a*, *b*). Finally, figures 15(*a*) and 15(*b*) reveal that the energy obtained by the subharmonic two-dimensional mode in both types of instability is transferred from the (0, 0) mode (the solid line with +). In H-type instability (figure 15*b*) the initial energy transfer from the (0, 0) mode to the $(\frac{1}{2}\omega, 0)$ mode increases rapidly as the flow develops downstream and its interaction with the oblique modes causes the rapid growth of the $(0, \beta)$ and (ω, β) modes (figure 12*b*). In K-type instability, the magnitude of the $(\frac{1}{2}\omega, 0)$ mode remains small, inhibiting the downstream growth of the subharmonics (figure 12*a*).

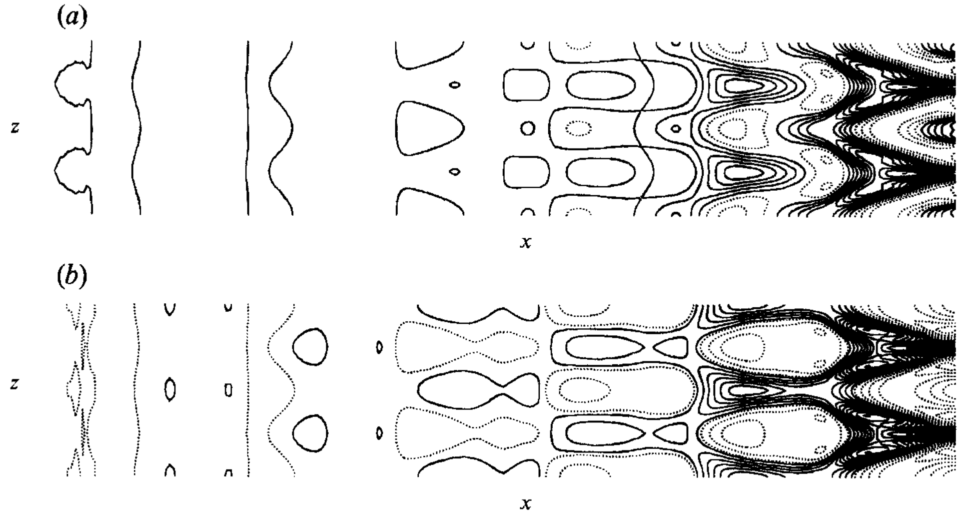

FIGURE 16. Contours of ω_z' in the (x, z)-plane near the critical layer, $y \approx 0.85$. (*a*) Case II-K: contour levels range from -1.0 to 0.4; (*b*) Case II-H: contour levels range from -1.15 to 0.5. The flow direction is from left to right, the spanwise length of the domain is doubled in order to depict the pattern of Λ-vortices, and $L_x = 33$. Solid and dashed contours denote negative and positive levels, respectively.

3.5. *Effects of high initial amplitudes and large spanwise wavenumbers*

In figures 16(*a*) and 16(*b*), the development of the Λ-structures in the (x, z)-plane near the critical layer for cases II-K and II-H is presented. These figures reveal that with higher amplitudes and larger spanwise wavenumber, Λ-vortices develop with comparable strength at the same streamwise location for both H- and K-type initial conditions. This development can also be observed in the x-distributions of u' Fourier amplitudes (figure 17*a*, *b*) which exhibit a strong amplification of the dominant three-dimensional mode for each case (i.e. the $(\frac{1}{2}\omega, \beta)$ mode – curve B, in H-type instability and the (ω, β) mode – curve C, in K-type instability) which eventually exceed the amplitude of the two-dimensional $(\omega, 0)$ mode. The comparable growth rates of the H- and K-type disturbances at large β is in accordance with the boundary-layer studies of Herbert (1988, 1991) and Spalart & Yang (1987) which suggests that with increasing β the differences between the growth rates of H- and K-type instabilities decrease. However, the strong amplitude dependency of this phenomenon in channel flows revealed in the present study has not been captured by previous temporal models. For H-type instability (case II-H), the flow development is again biased towards the upper wall as expected from the large spanwise wavenumber of the initial conditions.

The Fourier amplitude distributions also reveal a dip in the mean $(0, 0)$ perturbation mode for both cases, occurring at about the same x-location (curve E in figure 17*a*, *b*). For high-amplitude H-type instability (case II-H), the $(\frac{1}{2}\omega, 0)$ two-dimensional mode and the $(0, \beta)$ and (ω, β) three-dimensional modes have strong growth rates similar to the low-amplitude case (I-H). For the high-amplitude K-type initial conditions (case II-K), the $(\frac{1}{2}\omega, 0)$ mode has a higher amplitude and stronger growth rate than in case I-K, causing high growth rates of the subharmonic modes.

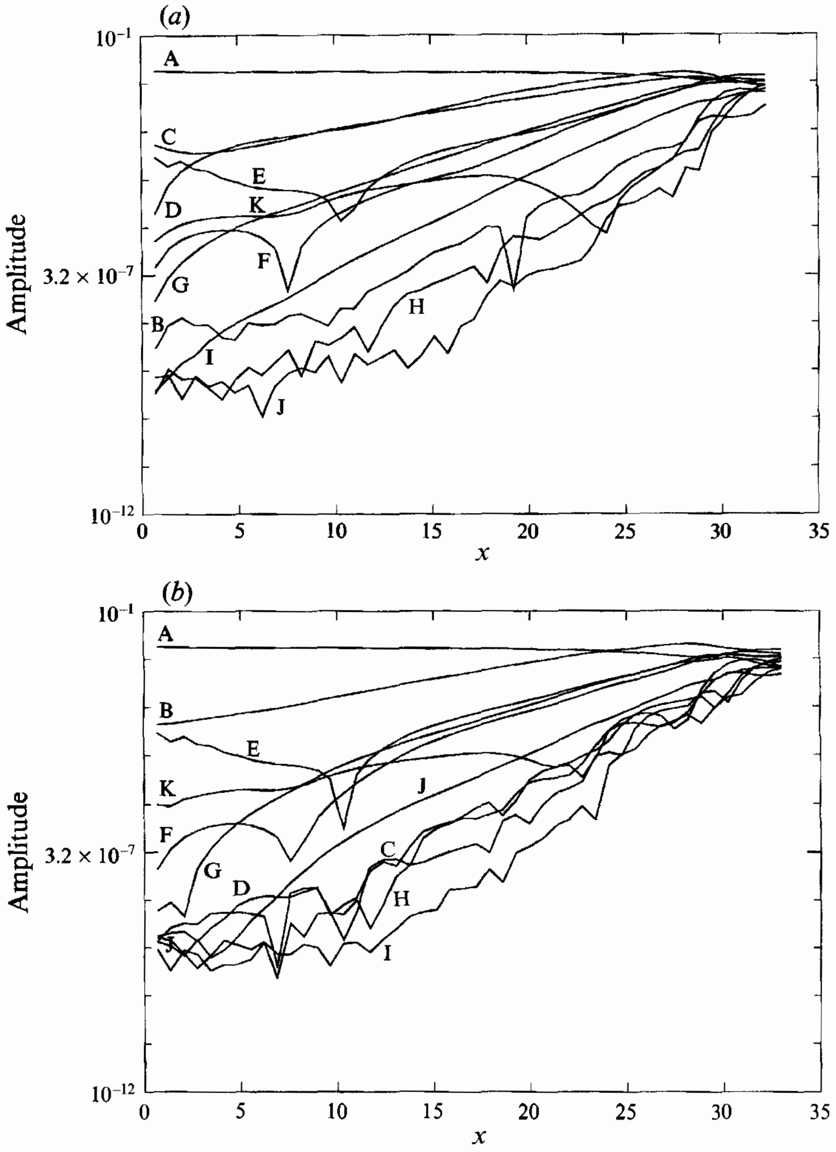

FIGURE 17. Streamwise distributions of Fourier amplitudes at $y \approx 0.85$. (*a*) Case II-K; (*b*) Case II-H. A, $(\omega, 0)$; B, $(\frac{1}{2}\omega, \beta)$; C, (ω, β); D, $(0, \beta)$; E, $(0, 0)$; F, $(0, 2\beta)$; G, $(\omega, 2\beta)$; H, $(\frac{1}{2}\omega, 2\beta)$; I, $(\omega, 3\beta)$; J, $(\frac{1}{2}\omega, 3\beta)$; and K, $(\frac{1}{2}\omega, 0)$.

4. Conclusions

In this study, the spatial evolution of H- and K-type secondary instability in plane channel flow was simulated by numerically integrating the three-dimensional, time-dependent, incompressible Navier–Stokes equations. Both types of secondary instability were initiated by a wave triad consisting of a two-dimensional T–S wave and a three-dimensional oblique wave pair. Comparisons were made between the quantitative and qualitative characteristics of the H- and K-type instabilities and between spatial and temporal computational approaches. For K-type instability, spanwise and normal distributions of u'_{rms} reveal excellent qualitative and quantitative agreement with experiments (Nishioka *et al.* 1980). The present results also demonstrate good qualitative agreement with the flow visualization experiments of Ramazanov (1985) for H-type instability.

For the inflow parameters imposed in these simulations, several interesting features were observed. In the nonlinear development stage of H-type instability, the spatial evolution of the disturbances was biased towards one wall, instead of simultaneous transition on both walls as observed in K-type instability. The biased behaviour in H-type instability is in accordance with both theoretical analyses and temporal simulations under comparable spanwise wavelengths used in the present work. In the current simulations, at low amplitudes of the perturbations, H-type instability exhibited higher growth than the K-type. This observation is in contrast to several temporal simulations in which H-type instability was found to be weaker than K-type regardless of the initial amplitudes and the spanwise wavenumber. At higher initial amplitudes, the present simulations revealed that the growth rates of the two types of secondary instability were comparable.

The present spatial simulations also differed from temporal studies in that for H-type instability there is a significant increase in the energy of the first spanwise harmonic, $(0, \beta)$, and the fundamental mode, (ω, β). These are excited by the nonlinear interactions of the $(\frac{1}{2}\omega, \pm\beta)$ oblique modes with the $(\frac{1}{2}\omega, 0)$ mode which obtains its energy directly from the mean mode. The subharmonic two-dimensional mode is also present in K-type instability and also obtains its energy from the mean mode. While its growth rate remains small for low-amplitude initial conditions, for high amplitudes it sustains significant growth and has a high rate of energy transfer to the subharmonic three-dimensional modes as the flow reaches the breakdown stage. A spectral energy analysis revealed that energy transfer from the mean to two-dimensional mode goes through a minimum which closely corresponds to a dip observed in the amplitude of the $(0,0)$ mode. This dip appeared further upstream in H-type instability than in K-type instability for low initial amplitudes, while for high initial amplitudes the dip appeared at about the same streamwise locations for both types of instability. In agreement with previous temporal studies, high energy transfer from the mean to the three-dimensional modes and net energy transfer from the three-dimensional modes to the two-dimensional mode were observed.

The authors would like to thank Bart A. Singer for his helpful comments and James A. Fein for his continued interest in this work. The authors also gratefully acknowledge the insightful comments of the anonymous referees. This work was supported by NASA Grant NAG-1-1161 and ONR Grant ONR00014-91-J-01086.

REFERENCES

ASAI, M. & NISHIOKA, M. 1989 Origin of the peak–valley wave structure leading to turbulence. *J. Fluid Mech.* **208**, 1.

BIRINGEN, S. 1984 Final stages of transition to turbulence in plane channel flow. *J. Fluid Mech.* **148**, 413.

BIRINGEN, S. 1987 Nonlinear structures of transition in plane channel flow. *Phys. Fluids* **30**, 3359.

BIRINGEN, S. 1990 Numerical simulation of non-linear structures in the final stages of transition in plane channel flow. *AIAA J.* **28**, 365.

CROSWELL, J. W. 1985 On the energetics of primary and secondary instabilities in plane Poiseuille flow. MS thesis, Va. Polytech. Inst. State University.

DANABASOGLU, G. 1992 Spatial simulation of transition in wall-bounded shear flows: Active control and effects of surface roughness. PhD thesis, University of Colorado.

DANABASOGLU, G. & BIRINGEN, S. 1990 A Chebyshev matrix method for the spatial modes of the Orr–Sommerfeld equation. *Intl J. Numer. Meth. Fluids* **11**, 1033 (also *NASA CR*-4247, 1989).

DANABASOGLU, G., BIRINGEN, S. & STREETT, C. L. 1990 Numerical simulation of spatially-evolving instability. In *Instability and Transition* (ed. M. Y. Hussaini & R. G. Voight), pp. 394–407. Springer.

DANABASOGLU, G., BIRINGEN, S. & STREETT, C. L. 1991 Spatial simulation of instability control by periodic suction blowing. *Phys. Fluids* A **3**, 2138.

FASEL, H. 1989 Numerical simulation of instability and transition in boundary layer flows. In *Laminar–Turbulent Transition* (ed. D. Arnal & R. Michel), pp. 587–598. Springer.

FASEL, H. & BESTEK, H. 1980 Investigation of nonlinear, spatial disturbance amplification on plane Poiseuille flow. In *Laminar–Turbulent Transition* (ed. R. Eppler & H. Fasel), pp. 173–185. Springer.

HERBERT, TH. 1983*a* Secondary instability of plane channel flow to subharmonic three-dimensional disturbances. *Phys. Fluids* **26**, 871.

HERBERT, TH. 1983*b* Subharmonic three-dimensional disturbances in unstable plane shear flows. *AIAA Paper* 83-1759.

HERBERT, TH. 1988 Secondary instability of boundary layers. *Ann. Rev. Fluid Mech.* **20**, 487.

HERBERT, TH. 1991 Exploring transition by computer. *Appl. Numer. Maths* **7**, 3.

HUSER, A. & BIRINGEN, S. 1992 Calculation of two-dimensional shear-driven cavity flow at high Reynolds numbers. *Intl J. Numer. Meth. Fluids* **14**, 1087.

KACHANOV, YU. S., KOZLOV, V. V. & LEVCHENKO, V. YA. 1978 Nonlinear development of a wave in a boundary layer. *Fluid Dyn.* **12**, 383.

KACHANOV, YU. S. & LEVCHENKO, V. YA. 1984 The resonant interaction of disturbances at laminar–turbulent transition in a boundary layer. *J. Fluid Mech.* **138**, 209.

KIM, J. & MOSER, R. D. 1989 On the secondary instability in plane Poiseuille flow. *Phys. Fluids* A **1**, 775.

KLEBANOFF, P. S., TIDSTROM, K. D. & SARGENT, L. M. 1962 The three-dimensional nature of boundary-layer instability. *J. Fluid Mech.* **12**, 1.

KLEISER, L. 1982 Spectral simulations of laminar–turbulent transition in plane Poiseuille flow and comparisons with experiments. In *8th Intl Conf. on Numerical Methods in Fluid Dynamics, Aachen 1982*. Lecture Notes in Physics, Vol. 170, p. 280. Springer.

KLEISER, L. & SCHUMANN, U. 1984 Spectral simulations of the laminar–turbulent transition process in plane Poiseuille flow. In *Spectral Methods for Partial Differential Equations* (ed. R. G. Voight, D. Gottlieb & M. Y. Hussaini), pp. 141–163. SIAM.

KLEISER, L. & ZANG, T. A . 1991 Numerical simulation of transition in wall-bounded shear flows. *Ann. Rev. Fluid Mech.* **23**, 495.

KONZELMANN, U., RIST, U. & FASEL, H. 1989 Numerical investigation of the effects of longitudinal vortices on the onset of transition in a flat plate boundary layer. *AGARD FDP CD* 438, pp. 7/1–7/13.

KOZLOV, V. V. & RAMAZANOV, M. P. 1984 Development of finite-amplitude disturbances in Poiseuille flow. *J. Fluid Mech.* **147**, 149.

KRIST, S. E. & ZANG, T. A. 1987 Numerical simulation of channel flow transition: Resolution requirements and structure of the hairpin vortex. *NASA Tech. Paper* 2667.

LAURIEN, E. & KLEISER, L. 1989 Numerical simulation of boundary-layer transition and transition control. *J. Fluid Mech.* **199**, 403.

MAY, C. L. & KLEISER, L. 1985 Numerical simulation of subharmonic transition in plane Poiseuille flow. *Bull. Am. Phys. Soc.* **30**, 1748.

NISHIOKA, M., ASAI, M. & IIDA, S. 1980 An experimental investigation of the secondary instability. In *Laminar–Turbulent Transition* (ed. R. Eppler & H. Fasel), pp. 37–45. Springer.

NISHIOKA, M., ASAI, M. & IIDA, S. 1981 Wall phenomena in the final stage of transition to turbulence. In *Transition and Turbulence* (ed. R. E. Meyer), pp. 113–126. Academic.

NISHIOKA, M., IIDA, S. & ICHIKAWA, Y. 1975 An experimental investigation of the stability of plane Poiseuille flow. *J. Fluid Mech.* **72**, 731.

ORSZAG, S. A. & KELLS, L. C. 1980 Transition to turbulence in plane Poiseuille flow and plane Couette flow. *J. Fluid Mech.* **96**, 159.

ORSZAG, S. A. & PATERA, A. T. 1983 Secondary instability of wall-bounded shear flows. *J. Fluid Mech.* **128**, 347.

PATERA, A. T. 1984 Spectral methods for spatially evolving hydrodynamic flows. In *Spectral Methods for Partial Differential Equations* (ed. R. G. Voight, D. Gottlieb & M. Y. Hussaini), pp. 239–256. SIAM.

PELTIER, L. J., BIRINGEN, S. & CHAIT, A. 1990 Application of implicit numerical techniques to the solution of the three-dimensional diffusion equation. *Numer. Heat Transfer* **B 18**, 205.

RAMAZANOV, M. P. 1985 Development of finite-amplitude disturbances in Poiseuille flow. In *Laminar–Turbulent Transition* (ed. V. V. Kozlov), pp. 183–190. Springer.

SARIC, W. S., KOZLOV, V. V. & LEVCHENKO, Y. YA. 1984 Forced and unforced subharmonic resonance in boundary-layer transition. *AIAA Paper* 84-0007.

SINGER, B. A., FERZIGER, J. H. & REED, H. L. 1987 Numerical simulation studies of laminar-turbulent transition in the plane channel. *Rep.* TF-31. Stanford University.

SINGER, B. A., REED, H. L. & FERZIGER, J. H. 1989 The effect of streamwise vortices on transition in the plane channel. *Phys. Fluids* A 1, 1960.

SPALART, P. R. & YANG, K.-S. 1987 Numerical study of ribbon-induced transition in Blasius flow. *J. Fluid Mech.* **178**, 345.

STREETT, C. L. & HUSSAINI, M. Y. 1986 Finite length effects in Taylor–Couette flow. *ICASE Rep.* 86-59.

STREETT, C. L. & MACARAEG, M. G. 1989 Spectral multi-domain for large-scale fluid dynamic simulations. *Appl. Numer. Maths* **6**, 123.

TANI, I. 1969 Boundary-layer transition. *Ann. Rev. Fluid Mech.* **11**, 169.

ZANG, T. A. & HUSSAINI, M. Y. 1985 Numerical experiments on subcritical transition mechanisms. *AIAA Paper* 85-0296.